SAND2020-0069J

Mesoscale Modeling of Hypervelocity Impacts using the CTH Shock Physics Code

Stephanie N. Q. Bouchey* and Jeromy T. Hollenshead
Sandia National Laboratories, PO Box 5800 Mail Stop 1185, Albuquerque, New Mexico 87113
*corresponding author, email: snquint@sandia.gov

ABSTRACT

Material fragmentation after a hypervelocity impact is important to predictive electro-optical and infrared (EO/IR) modeling. Successful comparisons with data require that hot, submicron fragments are generated in such impacts; however, experimental data has so far been unable to produce fragments of this scale. The purpose of this work was to investigate how modeling assumptions of macro-scale, bulk materials might influence the generation of debris in hypervelocity impacts and ultimately the predicted EO/IR signatures of these debris clouds. Sphere-on-plate impact simulations simplified the comparison of different modeling approaches. In one set of simulations, materials were modeled with the traditional, bulk approach. Those results were compared to simulations run with the mesoscale material grain structure explicitly modeled. This study focused on the comparison of two parameters that are tied directly to the EO/IR signature: strain rate at failure (a proxy for debris fragment size) and material temperature. Interfaces between grains, here due to void insertion, resulted in the most notable change in both the strain rate at failure and material temperature. Shock reflections from grain-void interfaces induced higher strain rates and material temperatures, and it is expected that similar effects may be produced from inclusions or dislocations in real materials. Thus, interfaces within a material may play an important role in producing smaller hot debris fragments that support the EO/IR predictive models of hypervelocity impacts.

KEYWORDS

Debris generation, hypervelocity impact, mesoscale modeling, EO/IR signature, CTH

HIGHLIGHTS

- Small, hot impact-generated fragments produce electro-optical/infrared signatures
- Mesoscale grain structure may affect strain rate and temperature (thus, signatures)
- Grain interfaces increase strain rate and temperature; results may improve models

1. INTRODUCTION

The purpose of this effort was to investigate the modeling assumptions that affect the generation of debris in hypervelocity impact simulations. Hypervelocity impact fragmentation is of interest to many fields, but this study was particularly motivated by that of electro-optical and infrared (EO/IR) signature modeling. EO/IR signatures that are generated in hypervelocity impacts originate from small, hot debris and are difficult to match in standard laboratory experiments and computational models [e.g., 1-2]. System-level simulations rely on sub-grid fragmentation theories in order to predict micro-debris, but little data exists to validate such models, especially at high strain rates [3-7].

The contribution detailed herein explores the effects of material modeling techniques on key parameters that affect EO/IR signatures: strain rate at failure and material temperature. Strain rate at failure is a proxy for fragment size. Specifically, this study used the Grady-Kipp fragmentation model, which describes different fragmentation regimes in which spall is dominated by either fracture toughness (Equation 1), flow stress (Equation 2), or liquid spall (Equation 3) when temperatures are high enough to melt the material [8-12].

$$S = \left(\frac{\sqrt{24}K_c}{\rho c \dot{\varepsilon}}\right)^{2/3} \tag{1}$$

$$S = \left(\frac{1.2Y}{\rho \dot{\varepsilon}^2}\right)^{1/2} \tag{2}$$

$$S = \left(\frac{48\gamma}{\rho\dot{\varepsilon}^2}\right)^{1/3} \tag{3}$$

where S is the fragment diameter, ρ is the density, $\dot{\varepsilon}$ is the strain rate, c is the sound speed, γ is the constant value of the surface tension, Y is the temperature and strain-rate dependent yield strength, K_c is the fracture toughness. The latter variables Y and K_c are defined in Kipp et al. [11]. Fragment size is dependent on the inverse of strain rate, or the inverse of the square of strain rate in the case of the flow stress and liquid spall regimes; and so, as strain rates increase in hypervelocity impacts, smaller debris sizes are expected.

Furthermore, material temperature directly affects the resulting EO/IR signatures. The Stefan-Boltzmann Law (Equation 4) can be applied as an example.

$$P = \sigma A T^4 \tag{4}$$

where P is the radiated power, A is the radiating area, σ is the Stefan constant, and T is the temperature. Thermal energy is proportional to the fourth power of temperature. In terms of hypervelocity impact modeling, as material temperatures increase, the thermal energy and therefore radiative power output significantly increases, which results in higher observed signatures.

Strain rate at failure and material temperature are intimately tied to the ultimate EO/IR signature of a hypervelocity impact; thus, this study focused on gaining a better understanding of how these parameters change in impact models. The first part of this investigation explored variations in strain rate at failure and material temperature in the traditional bulk (homogeneous) continuum approach to modeling. As most system-level simulations use this bulk approach, this initial study both served as a baseline and demonstrated the underlying physics of the hypervelocity impact problem. Problem resolution, in addition to impactor size, shape, and speed were tested.

The second part of this investigation explored the effect on strain rate at failure and material temperature of explicitly modeling the grain structure of materials. The mesoscale modeling approach is widely used for granular and reactive materials [e.g. 13-14] and has been used in metals [e.g. 15-16]. This work takes the approach of the latter with a new application of mesoscale modeling to assess the effect of grain structure on shock-induced strain rates and temperatures. A variety of studies examined the effect of changing material properties, such as spall strength, yield strength, and different types of material interfaces. It is hypothesized that the explicit modeling of grains, especially in the presence of void and varying grain properties, may lead to differences in predicted strain rates and material temperatures (locally higher) associated with the grain boundaries. Such an effect may lead to smaller predicted fragment sizes and hotter fragments, respectively, than when using the traditional bulk modeling approach, and therefore may provide improved understanding of modeling fragmentation in hypervelocity impacts.

2. METHODS

Computational modeling was performed at Sandia National Laboratories, New Mexico using the shock physics analysis package, CTH. CTH is a family of codes developed at Sandia National Laboratories specifically for modeling large-deformation and strong-shock problems in multiple dimensions and with multiple kinds of materials [17-18]. The current investigation was based on a two-dimensional (2D) description of the sphere-on-plate problem. In CTH, this problem was modeled as a 2D cylindrical geometry with x-y coordinates. A 2D circle is representative of a sphere in three-dimensions (3D), while a 2D square is a 3D cylinder or a cylindrical plate. In order to compare the two different modeling approaches, two computational designs were required. The first utilized the traditional *bulk*, macro-scale description of the materials in which both the target and impactor were

represented as two separate, bulk materials. In the second design, the target and projectile both contained an explicit *mesoscale* grain structure representative of a metal like aluminum.

2.1 Nominal Problem Design

The nominal problem design was a sphere impacting a semi-infinite flat plate target at 4 km/s. Although the bulk model was developed first, many of the system characteristics were driven by the expected requirements for the mesoscale model description. For example, domain and impactor size were driven by the size of aluminum grains and their associated resolution requirements. Analysis of a pure aluminum sample defined the short axis of an aluminum grain as ~14 μm, as estimated from Nakai and Itoh [19] and Case and Horie [16] (for copper). In hydrocodes, the choice of resolution is important. Material shapes and boundaries must have enough resolution to accurately represent the physics occurring (flow variations, shock waves, etc.) [20]. For Eulerian codes like CTH, a rule of thumb is to have at least two cells per material thickness (more if possible) in order to resolve the shock wave, which is spread over multiple cells from artificial viscosity [17-18, 20]. To effectively resolve aluminum grains, an initial flat-mesh resolution of at least 7 μm was required. Such high resolution necessitated exceptionally small impactors to incorporate a sphere-on-plate geometry. Initial studies evaluated a 1.4-mm diameter projectile (corresponding to 100 grains across), though a larger projectile (7-mm diameter, 500 grains across) was chosen for most of the remaining work. Figure 1 is a snapshot of the problem domain, where both projectile sizes are represented as black circles.

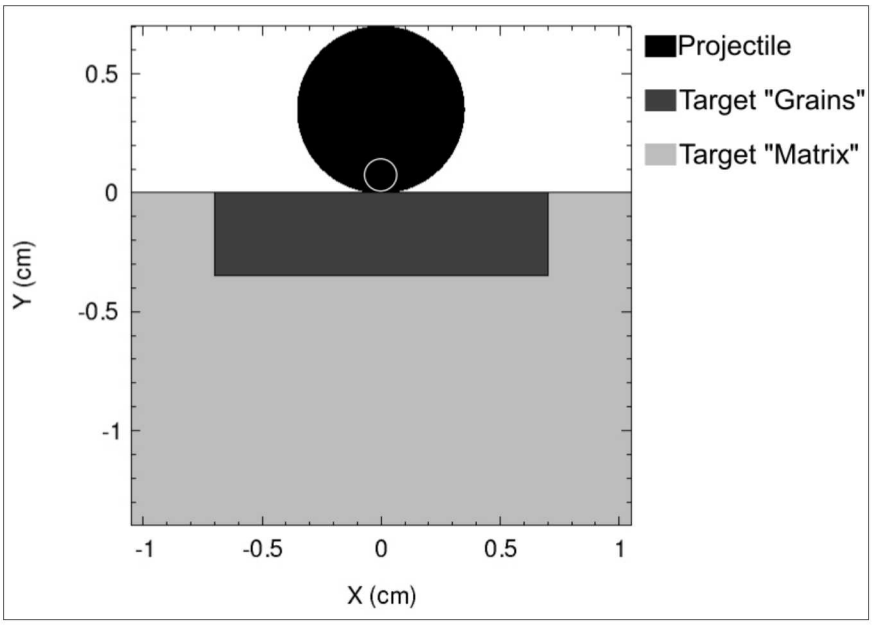

Figure 1 - Simulation domain with the three primary regions displayed in different shades. The nominal projectile size was 1.4 mm (small circle). The larger projectile (7 mm) was primarily used in the mesoscale study. The target area designed to contain grains in the mesoscale study is the dark gray rectangle, which is surrounded by the light gray solid target matrix area.

In order to reduce edge and boundary effects, the target was designed to be much larger than the projectile. Only half of the domain was modeled, and then mirrored around x=0 (an advantage of 2D, vertical impact calculations). Target measurements are given for the entire (mirrored) domain. The total target area was 70 mm wide by 70 mm deep (Figure 1 is zoomed in to the area of interest). The prohibitive computational expense of filling this entire area with grains was mitigated by dividing the target into two regions of interest (Figure 1). Schultz [21] demonstrated that an impactor will couple completely to a target layer that is only 0.25 times as thick as the diameter of the impactor. This study doubled the thickness found by Schultz [21] and modeled the "grains region" of the target to be 3.5 mm thick and 14 mm wide. In the bulk model design, this small target area was simply initialized a single material, whereas in the mesoscale simulations, this area was then filled with grains. The larger target domain (the "target matrix area") was a single, bulk material in all simulations.

Both the projectile and target were modeled using a tabular aluminum SESAME equation of state. Constitutive models included a Johnson-Cook viscoelastic strength model, a Johnson-Cook fracture model, and the Grady-Kipp fragmentation model. In order to provide some contrast between the projectile and target, different Johnson-Cook strength models and fracture pressures were used. The projectile was nominally modeled as Aluminum 1100 with a fracture/spall pressure of 124 MPa. The target was nominally modeled as Aluminum 7075 with a fracture/spall pressure of 575 MPa.

2.2 Mesoscale (Grains) Description

Traditional material descriptions within CTH are typically macro-scale and do not include any explicit grain structure representation. Consequently, a procedure to model and initialize grains within CTH was necessary. A MATLAB Monte Carlo simulation of 2D grain growth using a Q-state Potts model was used to generate a unit cell of grains, similar to the approach of Haghighat and Taheri [22]. The current configuration allows for eight different grain types in both the target and projectile (16 total materials). Each grain type was randomly distributed within the unit cell, and the entire cell was then scaled such that the average grain size was ~14 μm in diameter. Typical aluminum grains do not have a 1:1 aspect ratio due to treatments they undergo, but the initial study here retained the 1:1 aspect ratio for simplicity. Finally, this scaled unit cell was tiled repeatedly to generate the impact geometry (projectile and target grains areas), and the result was written out pixel by pixel in a form (DIATOM) that could be read by CTH (Figure 2).

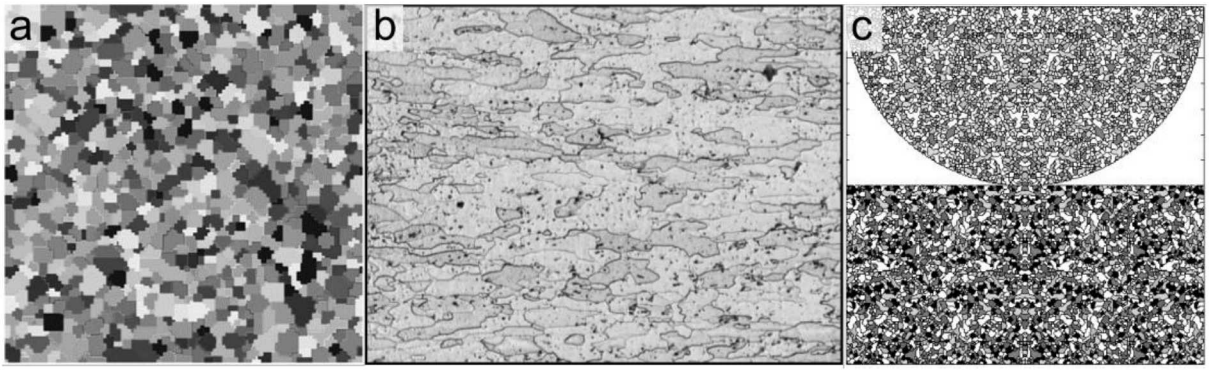

Figure 2 - A grain structure is produced in MATLAB using the Q-state Potts model of 2D grain growth (a), based on a pure aluminum sample [23] (image reproduced with permission) (b). The unit cell is then tiled to fill the projectile and grains area geometry in CTH (here the 1.4 mm projectile and grains area) (c). Note: images are not on the same scale.

Because this study is only 2D, some 3D details are lost. The grains are not near-spheres but are instead tori when extrapolated to 3D. Some expected inter-grain behavior is lost, such as the interaction of shock and rarefaction waves in the out-of-plane direction resulting in higher pressures than would be expected in the 3D case. However, the purpose of this work is to explore factors that may affect strain rate at failure and material temperature at the grain scale, and a 2D study is sufficient for this purpose. The goal is to bring awareness to and gain a better understanding of how assumptions made in traditional bulk (macro-scale) models might affect the answers that are obtained from the code. A 3D study is warranted to calibrate grain-scale effects and ultimately influence how bulk model simulations are performed.

2.3 Simulation Runtime and Processing

From the baseline macroscale (bulk) and mesoscale (grains) problem representations, a series of simulations were developed to investigate the sensitivity of the solution to parameters of interest. In total, over 30 simulations were run on the High-Performance Computing (HPC) clusters at Sandia National Laboratories with up to 256 processors each.

All simulations were run out to a time between 1-2 μs, which allowed the shockwave to reach (and extend beyond) the target grains area. The simulations were stopped before the reflected wave re-entered the target grains area.

Data, including Grady-Kipp strain rate at failure and material temperature, among others, were saved for each time step. At any given time, data can be written out to an ASCII text file for processing. Such a file was then assessed with a custom-build Python post-processor to calculate conservation metrics and generate cumulative distribution functions (CDFs) and histograms for any desired variable/property (here, strain rate at failure and material temperature vs. mass). These outputs served as the key metrics for comparisons between the various simulations.

3. RESULTS AND DISCUSSION

3.1 Bulk Model Analysis

The bulk model suite simulated a projectile striking a target within a larger target matrix. The target and matrix were both aluminum and had the same material properties. For contrast, the projectile was also aluminum but had slightly different material properties (see Section 2.1). The bulk model is the baseline with which to compare the explicit modeling of grains. An exploration of the physics in the problem was achieved through the following studies: resolution, impact velocity, projectile size, and projectile shape.

3.1.1 Resolution Study

Simulations of the impact of a 1.4-mm diameter projectile at 4 km/s allowed for testing the effect of resolution and evaluating the initial requirement of a 7-μm cell size. Five resolutions were assessed: 14.0, 7.0, 3.5, 1.75, and 0.875 μm. Table 1 lists the number of cells spanning the projectile for each resolution tested. The results of the resolution study can be compared through histograms and CDFs of strain rate at failure and material temperature,

taken at a given time for all simulations. Strain rate at failure and material temperature are recorded in each cell and then summed, binned, and plotted by material. Figure 3 is a series of plots of the results for the projectile, and Figure 4 contains the results for the target.

Table 1 - Projectile Resolution Comparison

Cells across projectile by resolution (Projectile Diameter = 1.4 mm)					
Resolution (µm)	14	7	3.5	1.75	0.875
No. cells across diameter	100	200	400	800	1600

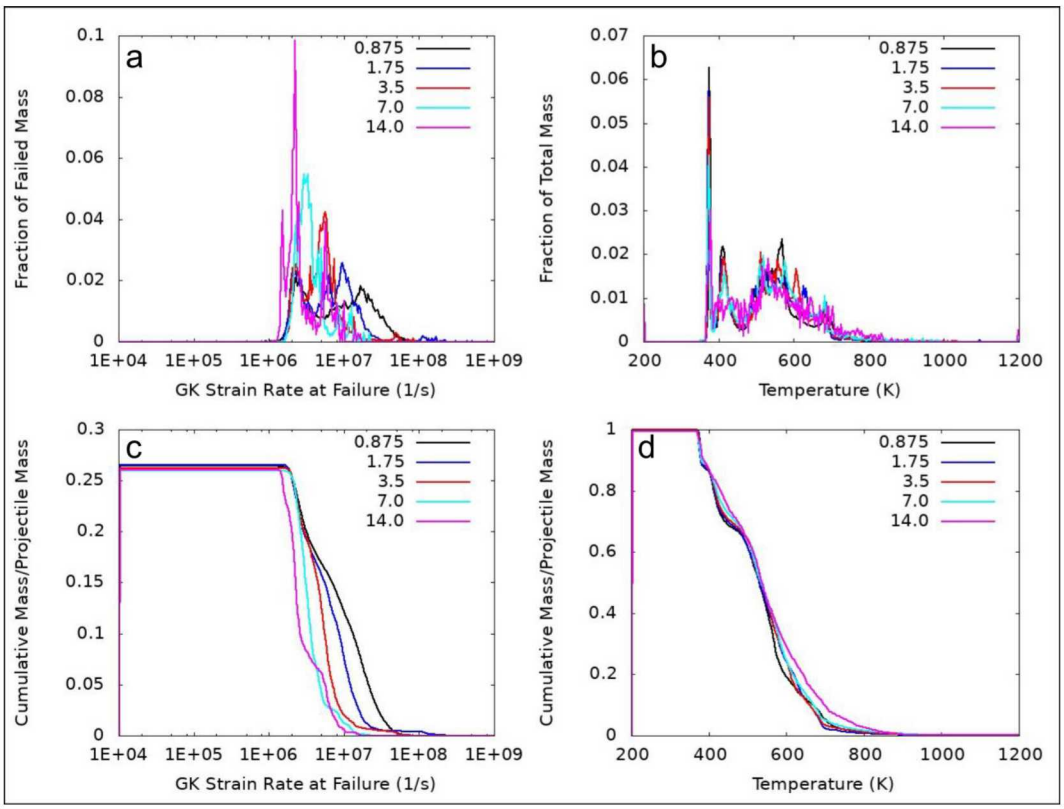

Figure 3 - Resolution Study Results (Projectile). Histograms of (a) strain rate at failure and (b) material temperature are compared with scaled cumulative mass (cumulative mass/projectile mass) for (c) strain rate and (d) material temperature. Each line represents a resolution (in µm) tested. Convergence is seen in termperature, but not strain rate. The 3.5-µm resolution mesh was chosen for the remaining calculations.

Figure 3 and Figure 4 compare histograms of strain rate at failure and material temperature in the projectile and target, respectively, for each of the resolutions tested.

Across the range of resolutions explored, material temperature appears to be converged but not the strain rate at failure. Grady-Kipp strain rate is dependent on resolution; thus, this result is not surprising. Higher resolution projectiles exhibit higher strain rates and a wider-spread bimodal distribution. Rise of the initial peak in strain rate at failure is the same for all resolutions except the coarsest (14 µm). This similarity suggests a resolution of 7.0 µm is sufficient. The increased computational cost of running at 3.5-µm resolution was reasonable so all remaining simulations were run at this level.

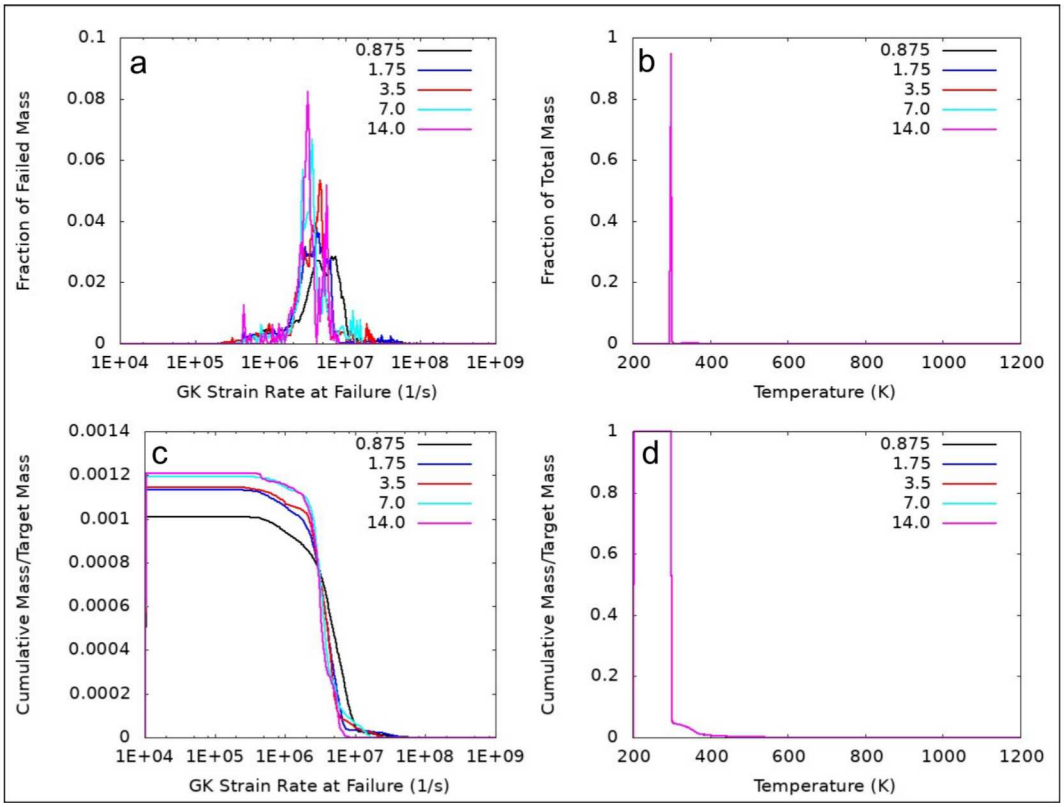

Figure 4 - Resolution Study Results (Target). Histograms of (a) strain rate at failure and (b) material temperature are compared with scaled cumulative mass for (c) strain rate and (d) material temperature. Each line represents a resolution (in µm) tested. Again, convergence is not observed in the strain rate plots, as expected from the Grady-Kipp fragmentation model. Temperature plots are punctuated by most material being at the reference temperature because the target matrix material was included.

Similar plots for the target reveal less variation in strain rate and little to no bimodality, which indicates that a property of the projectile (geometry, size, etc.), rather than of the material, is likely causing the variation in strain rate between resolutions. In the target (Figure 4), strain rate histograms generally seem to overlap for mid-range resolutions of 3.5 μm and 1.7 μm. Material temperature plots for the target are punctuated by most of the material at the initial temperature; hence, the techniques used for analysis of the projectile may not be as instructive for the target. Finite-thickness objects, like the projectile, are of interest for system-level simulations. For this reason, and because the target histograms and CDFs do not communicate significant additional information, they will not be included in the remainder of the bulk study results.

3.1.2 Projectile Size Study

The projectile size study tested the effects of projectile curvature and overall size relative to the domain. Figure 5 compares the four different size projectiles in CTH pressure plots. An equivalent stop time (Table 2) ensured consistency between the different sized projectiles. The equivalent time is the time at which the projectile would travel one projectile-diameter into the target, based only on speed. Strength in the materials thus prevents the projectile from penetrating the target at the equivalent time. The impact velocity for each projectile size was 4 km/s. Only the largest projectile developed a shockwave that reached the edge of the domain. In this case the boundary condition chosen produced a rarefaction wave back into the target, but the rarefaction wave had not reached the grains area and did not affect the results at the designated time.

Table 2 - Projectile Size and Equivalent Stop Time

Projectile Diameter mm	Stop Time µs
0.7	0.175
1.4	0.35
3.5	0.875
7	1.75

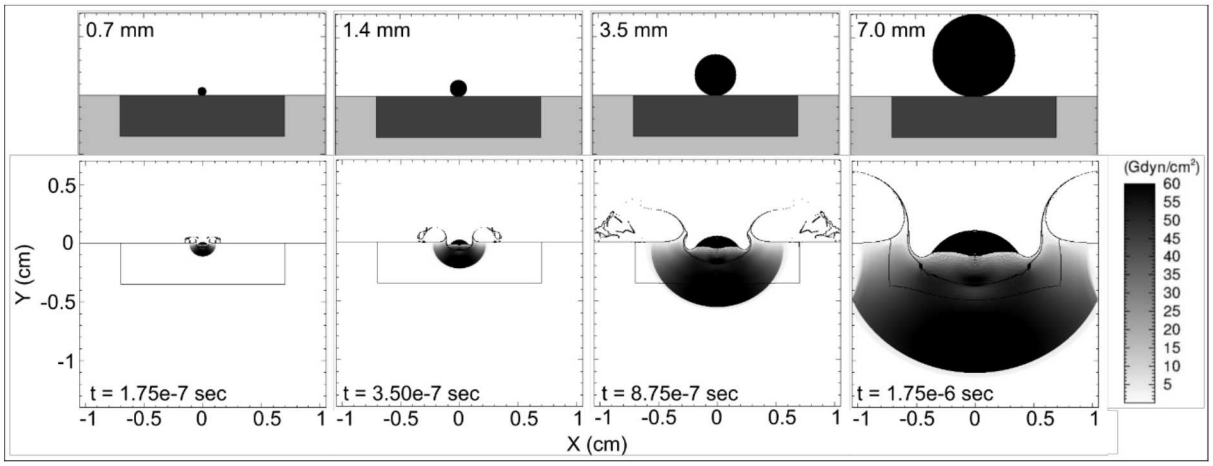

Figure 5 - Projectile Size Comparison. Pressure plots (bottom row) for each projectile size (shown at top with half of the domain) at equivalent time (see Table 2). Only the largest projectile produced a shockwave that reached the edge of the domain and developed a rarefaction wave. The simulation was stopped before the rarefaction interacted with the grains region.

Histograms and CDFs were evaluated at the equivalent times listed in Table 2. Figure 6 contains results for the projectile. The distance between the peaks in each strain rate histogram may be at least partially driven by transit time across the object (i.e., by a characteristic length scale, which is projectile diameter in this case). Onset of the strain rate histogram is clearly related to projectile size, as is the overall histogram shape. Interestingly, the temperature at which failure occurs is similar between all projectile sizes. This surprising temperature effect appears to be related to geometry scaling. Even though the projectile imparts more kinetic energy with increasing size, the volume of affected material also increases.

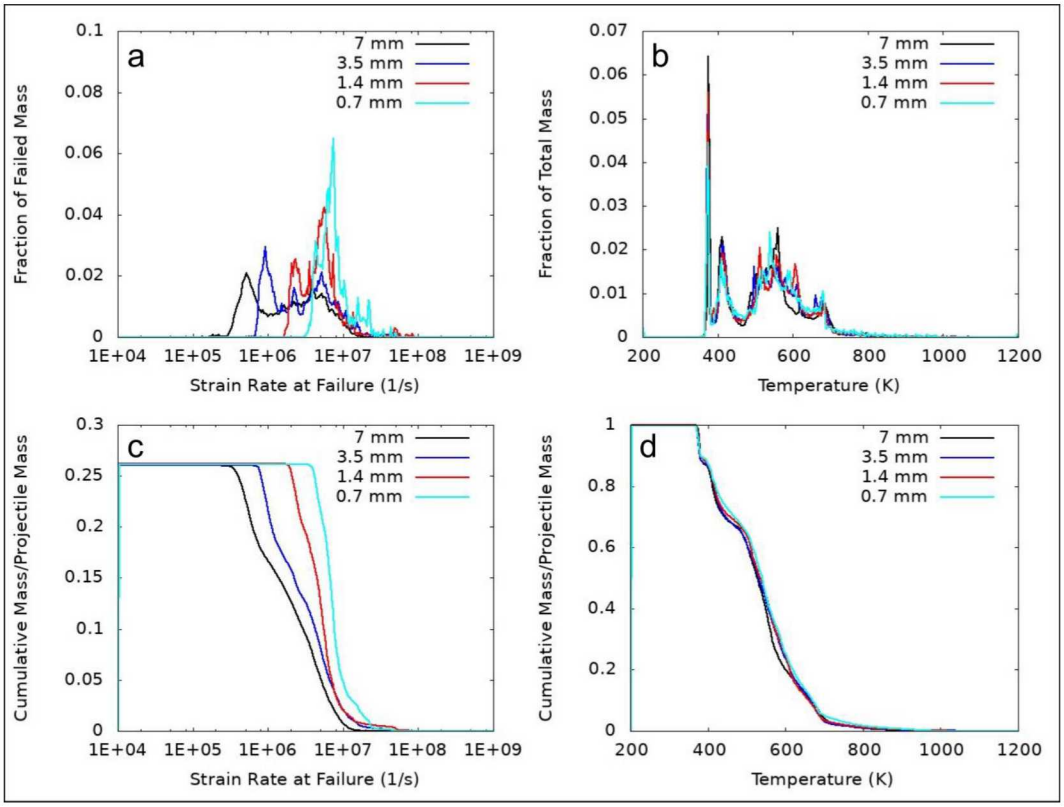

Figure 6 - Size Study Results (Projectile). Histograms for (a) strain rate at failure and (b) material temperature compared to equivalent scaled cumulative mass plots of (c) strain rate at failure and (d) material temperature. Strain rate onset is dependent on projectile size, as is the bimodality of the strain rate histogram. Interestingly, material temperature remains nearly unchanged with increasing projectile size, likely due to energy scaling.

3.1.3 Projectile Shape Study

Projectile shape and the effect it has on resulting strain rates at failure and material temperature is an important consideration, as well. Three additional models tested projectile shape by impacting a face-on cylinder, rather than a sphere, into the target at the nominal impact speed. Three different sizes of cylinders (of equal height and diameter, 7 mm, 1.4 mm, and 0.7 mm) allowed for a comparative study to the sphere size study, above. Results for the projectile are in Figure 7. A direct comparison of the 7-mm cylinder with the 7-mm diameter spherical projectile illuminates the significant effect of projectile shape (Figure 8).

The histogram plot in Figure 7 demonstrates that the bimodality seen in the strain rate histograms appears to be related to projectile curvature (in addition to the characteristic

length, as was seen in Section 3.1.2). A more step-like or punctuated strain rate at failure histogram is apparent in the larger cylinder impacts, which becomes especially evident in the direct comparison of projectile shape in Figure 8. In a sphere, rarefaction waves are immediately generated at the free surfaces and more quickly reduce the high shock pressures. The cylinders, comparatively, impact with more surface area. Shock waves from the impact can travel farther into the target and projectile before rarefaction waves from the edges of the cylinder propagate inward and reduce the shock pressures. For similar reasons, temperatures also shift higher for the cylinder impacts as compared to the spheres. The size of the cylinder, however, does not appear to influence temperature; this result was also seen in the sphere impacts.

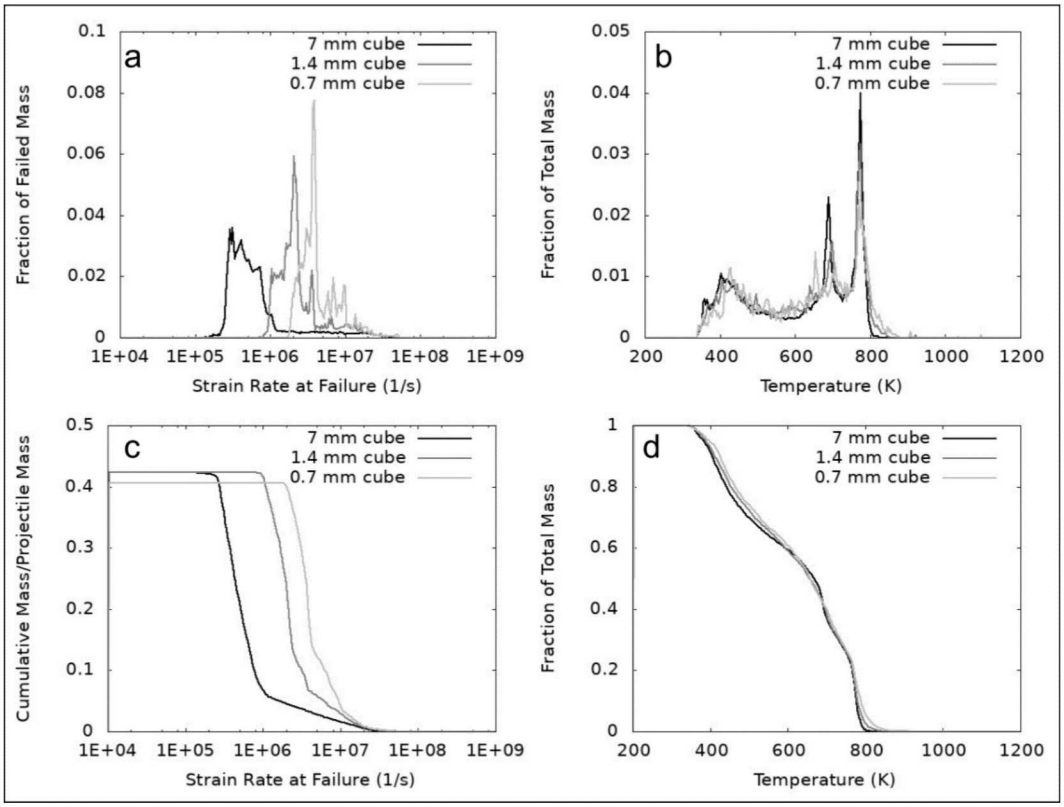

Figure 7 - Shape Study Results (Projectile). Histograms for (a) strain rate at failure and (b) material temperature compared to equivalent scaled cumulative mass plots of (c) strain rate at failure and (d) material temperature for three different projectile sizes. Here, projectiles were cylinders, rather than spheres. Strain rate onset is dependent on projectile size, as before, but the overall histogram shape is more step-like or pulsed than with spherical projectiles. As in Figure 6d, temperature appears not to be dependent on projectile size.

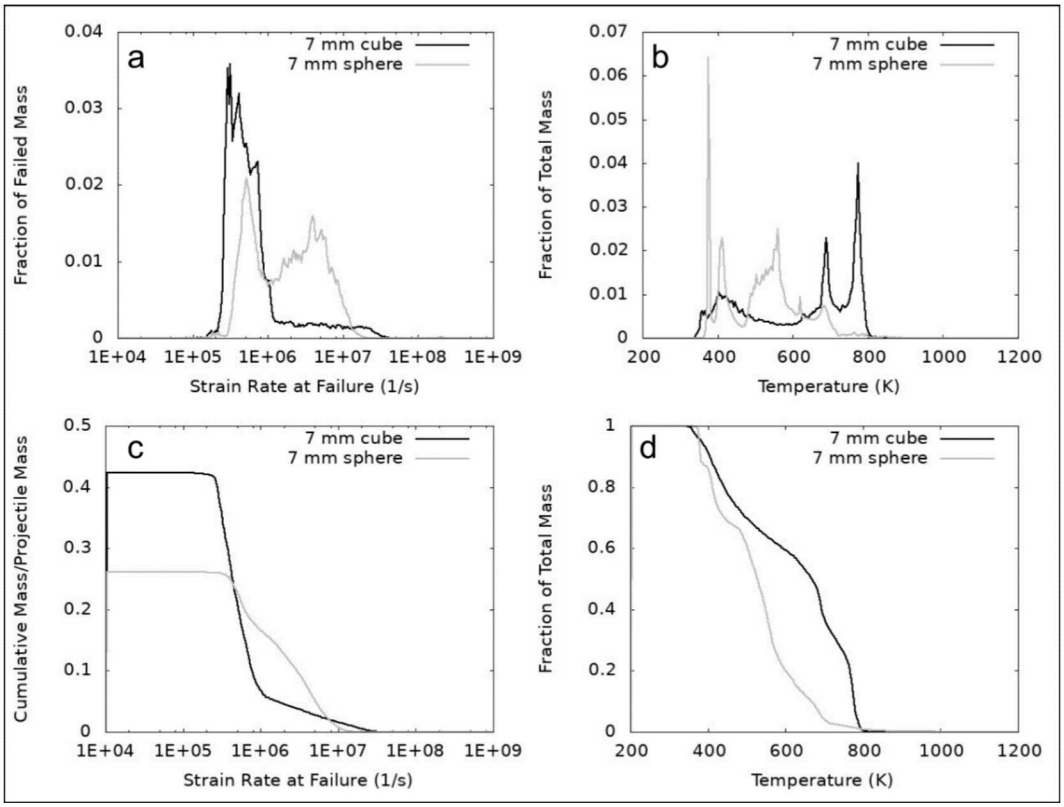

Figure 8 - Shape Study Results (Projectile, 7mm). The black line is the result for the 7-mm cylinder impact, and the gray line is the 7-mm sphere. Histograms for (a) strain rate at failure and (b) material temperature compared to equivalent scaled cumulative mass plots of (c) strain rate at failure and (d) material temperature for three different projectile sizes. Bimodality is lost in the cylinder impacts, and temperatures shift higher when compared to the sphere impacts.

3.1.4 Impact Velocity Study

Finally, two impact velocities, 4 km/s and 6 km/s, were tested on two different projectile sizes, 1.4-mm diameter and 7-mm diameter. Figure 9 is a plot of the histogram and CDF results for the projectile. Increases in impact velocity result in a shift to higher strain rates and temperatures, but overall shape and bimodality are not significantly affected. The temperature histogram is nearly unchanged by projectile size for impacts at the same speed (Figure 9b and d), which is consistent with the results of the shape and size studies above. Impact velocity clearly controls temperature in the projectile. To reduce complexity for the remainder of the simulations, only the nominal 4 km/s impact speed was chosen.

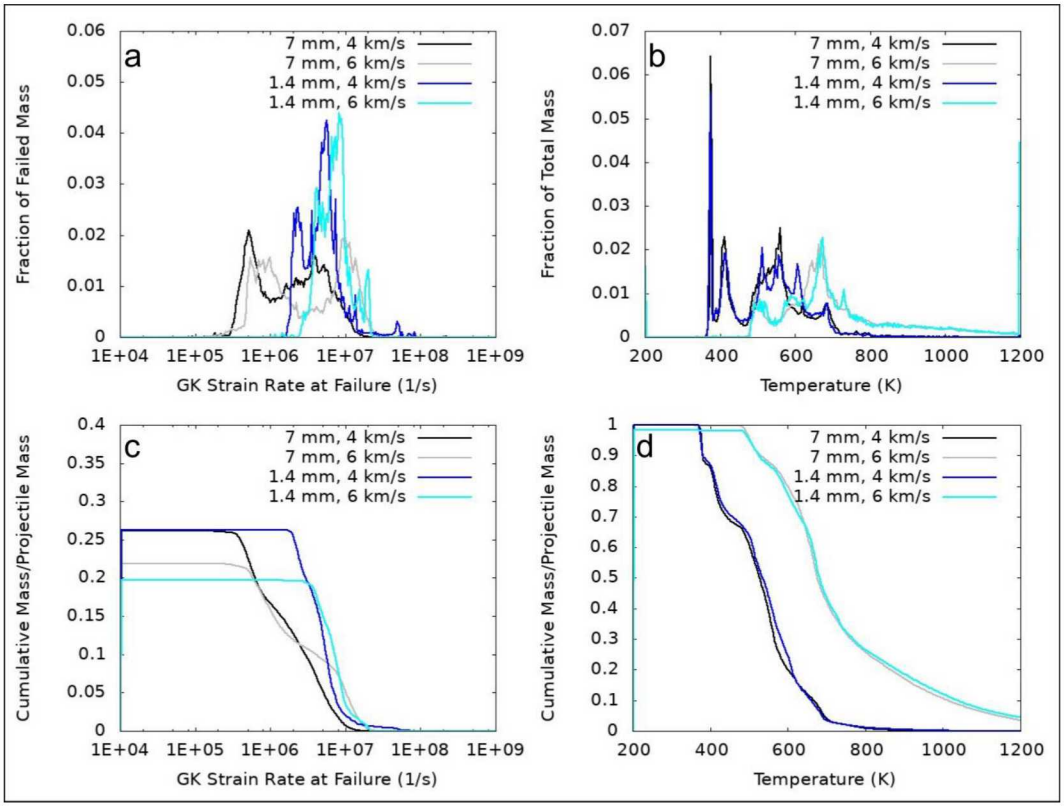

Figure 9 - Velocity Study Results (Projectile). Histograms for (a) strain rate at failure and (b) material temperature compared to equivalent scaled cumulative mass plots of (c) strain rate at failure and (d) material temperature. The 7-mm diameter sphere results are in black and gray; the 1.-mm diameter sphere results are in blue and cyan. Increased impact velocity (gray and cyan lines) clearly causes an increase in strain rate and temperature. At a given velocity, projectile size does not appear to have much of an effect, which is consistent with the shape and size studies, above. (For interpretation of the references to color in this figure legend, the reader is referred to the web version of this article.)

3.1.5 Summary

In summary, the bimodal distribution observed in projectile histograms of strain rate at failure appears to be related to projectile shape. The first peak appears to be driven by transit time across the object, which was controlled by projectile diameter in this case. The second peak seen in histograms of strain rate at failure appears to be unrelated to impact conditions. Only small changes were observed in the second peak due to the increase in impact speed or projectile size, which suggests a material property like sound speed is the controlling factor. Changing impactor material would be an excellent future test of this

hypothesis. Finally, reducing projectile size or increasing projectile velocity unsurprisingly results in increases to strain rate at failure and material temperature.

3.2 Mesoscale (Grains) Model Analysis

The mesoscale model analysis suite built upon the baseline impact problem of a spherical projectile impacting a semi-infinite target at 4 km/s. Here, the grain structure in both the projectile and the target "grains area" (see Figure 1) was explicitly modeled by the process outlined in Section 2.2. Each grain region was composed of a combination of different grain types, which were initialized in the hydrocode as separate materials. This technique enabled a range of discrete strength and failure properties to be specified across the grain types within the projectile and target.

Furthermore, based on results from the baseline bulk study, a resolution of 3.5 μm and a projectile size of 7 mm were chosen. Eight grain types (eight individually initialized materials), randomly distributed, comprised the projectile. The 7-mm projectile contained ~250,000 grains. Additionally, eight separate grain types comprised the "grains area" of the target, which was surrounded by the bulk "matrix area" of nominal target material. The grains area contained ~80,000 grains. This modeling approach enabled the following studies: bulk consistency, fracture strength distribution, yield strength distribution, slip interfaces, and void-related interfaces.

3.2.1 Bulk Consistency Study

The consistency study served as a numerical check and tested whether grain boundaries affect strain rate at failure or material temperature when compared to the bulk case. The nominal consistency test initialized all grain types in a geometry (the projectile or the target) to the same material properties, but each type was individually initiated in the

simulation code. For example, the projectile consisted of Materials 1-8. In a variation to this study, all grain types in a geometry were also initialized to have the same material properties, but the initialization was such that each grain type was defined as the same material. For example, Material 1 was repeated eight times in the projectile. A flat mesh ensured that cell size was consistent in each test.

A qualitative comparison between the nominal consistency test and the bulk case is shown through a plot of CTH pressure in Figure 10. Note that only part of the domain is shown. Modeling individual grains does not substantially affect the pressure results.

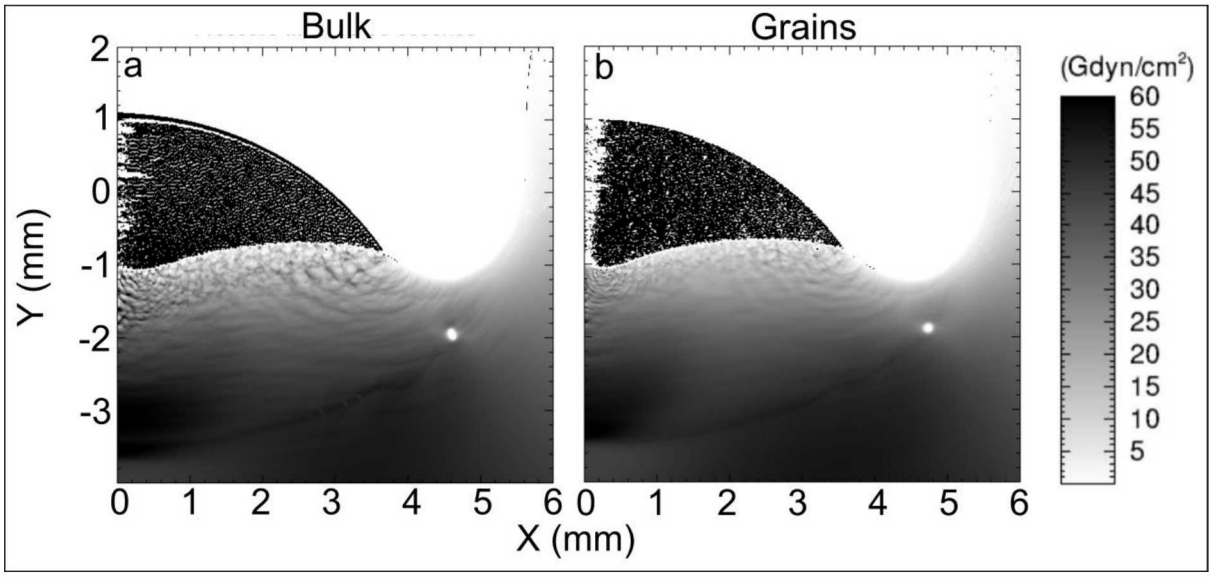

Figure 10 - Comparison of pressure plots (painted over black projectile) in the (a) bulk case and (b) the mesoscale consistency case for the 7-mm diameter projectile.

A more quantitative comparison between the simulations is recorded in histograms and CDFs, which document more subtle changes between the bulk and mesoscale simulations. Individual grains produce a noisy histogram profile when compared to the bulk case (see Figure 11a); however, the overall histogram range and shape is very similar in both cases. The noisy profile is attributed to discrete spatial sampling associated with examining a

single material, which exists as randomly distributed grains across the entire geometry. This discrete spatial sampling is expected to exhibit more variation than the bulk result, which samples the response of the entire geometry and incorporates a larger amount of material. An average of all grain types produces a less noisy profile. Compare the histogram for all grain types (shades of blue) and their average (dark gray) to the bulk case (black) in Figure 11b.

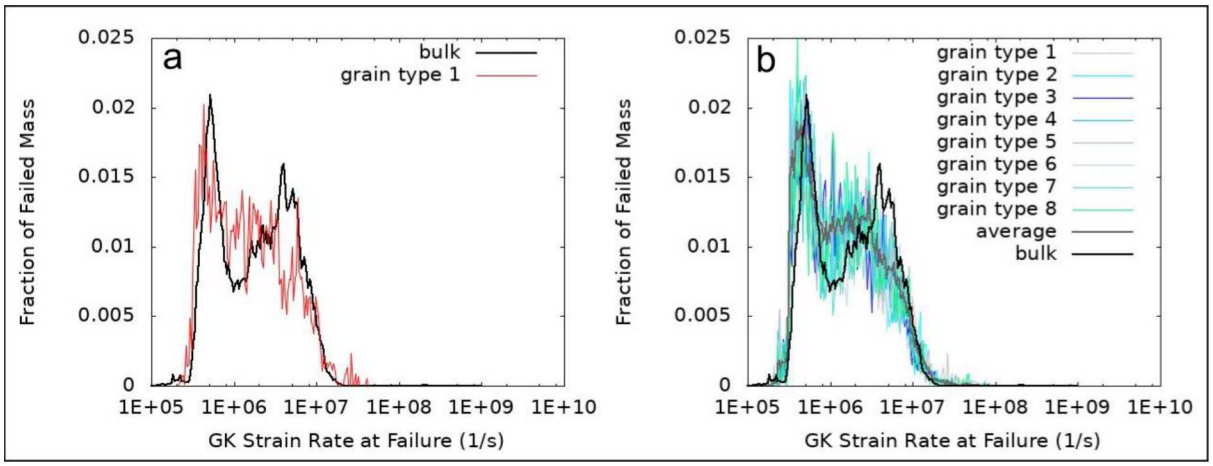

Figure 11 - (a) Single grain-type profile from the nominal consistency test (red line) compared to bulk case (black line) for the 7-mm diameter projectile. (b) All grain types plotted in blue and green hues compared to the average of the grain types (dark gray) and the bulk case (black) for the 7-mm diameter projectile. (For interpretation of the references to color in this figure legend, the reader is referred to the web version of this article.)

Despite grain type averaging, the profile does not match the bulk case to the extent expected. Even though each grain type (material) has the same properties and is therefore expected to produce a histogram very similar to the bulk histogram, deviation in the strain rates at failure from the bulk case exists. Because all material properties were the same between tests, homogenization of mixed cells cannot be the source of the discrepancy. These differences are attributed to numerical, rather than physical effects, such as the discrete sampling issue discussed above. Advection transport is material dependent and may also contribute to the noisy histograms. Nonetheless, for congruity between material modeling

technique studies, the remaining mesoscale studies will be compared to the nominal consistency test with grain type averaging.

3.2.2 Fracture Study

The occurrence of spallation in the simulations to date indicate that fracture strength is an important material property. Individual grains may be expected to have different fracture strengths than the bulk material. The question addressed by this study is whether varying fracture strength within grains might cause an increase in the resulting strain rate at failure and material temperature.

Values for the fracture strength of each of the eight grain types were chosen randomly from a normal distribution of fracture strengths centered on that of Aluminum 1100, 5.72E+9 dyn/cm^2. The distribution was produced based on the fracture strength of a variety of aluminum alloys, and therefore reduced the possible values to only those that would be plausible for aluminum. Results for this study can found be in Figure 12.

The inclusion of a fracture strength distribution within the grains resulted in an increase in the mass of material that failed at low strain rates when compared to the grains consistency result. No increase in higher strain rates was apparent, as the second peak remained similar between the two tests. Almost no change in temperature was noted, either. From these results, internally variable fracture strength is not expected to significantly affect fragment size, material temperature, or the EO/IR signatures of a hypervelocity impact.

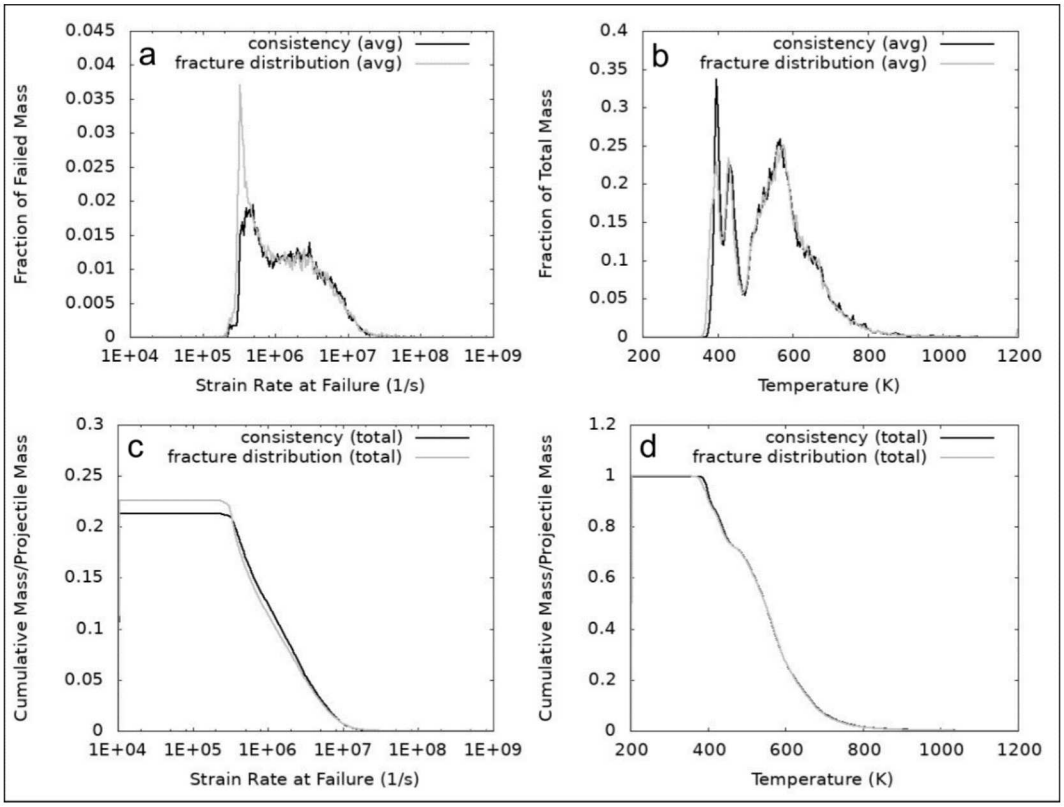

Figure 12 - Fracture Strength Study Results (Projectile). Comparison of the consistency case (black line) with the results from using a fracture strength distribution in the grains (gray line). Histograms for (a) strain rate at failure and (b) material temperature compared to equivalent scaled cumulative mass plots of (c) strain rate at failure and (d) material temperature. Fracture strength predominantly affects only the first peak in the strain rate at failure histogram (i.e. only low strain rates at failure). Higher strain rates, as well as material temperatures, are unaffected by the change in fracture strength.

3.2.3 Strength Study

Yield strength also varies from one aluminum alloy to another, and it is plausible that individual grains within a bulk piece of aluminum may also have variable yield strength. Simulations here used the Johnson-Cook yield strength, which is calculated with Equation 5 in CTH,

$$Y = \left(A + B{\varepsilon_p}^n\right)\left(1 + C \ln {\dot{\varepsilon}_p}^*\right)\left(1 - T^{*m}\right) \tag{5}$$

where ε_p is the equivalent plastic strain; $\dot{\varepsilon}_p^*$ is the plastic strain rate; T^* is the homologous temperature, $(T - T_{room})/(T_{melt} - T_{room})$; and A, B, C, m, and n are all material constants [24-26].

The fracture strength distribution from Section 3.2.2 was kept for the strength study. Additionally, a range of values for A, B, and C were found from various aluminum alloys [27]. Values for each material constant (A, B, and C) were chosen randomly from a normal distribution of plausible values centered at those for Aluminum 1100, very much like the process described in Section 3.2.2 above. All other material constants from Equation 5 remained as the defaults for Aluminum 1100.

As was seen in the fracture study, a change in the grain material yield strength properties did not have a substantial effect on strain rates or temperatures produced in the impact (Figure 13). In fact, overall less material failed at lower strain rates, and there was very little change in amount of material that failed at higher strain rates. Overall material temperature was also slightly lower. Again, these results imply that internally varying yield strength would not affect resulting EO/IR signatures.

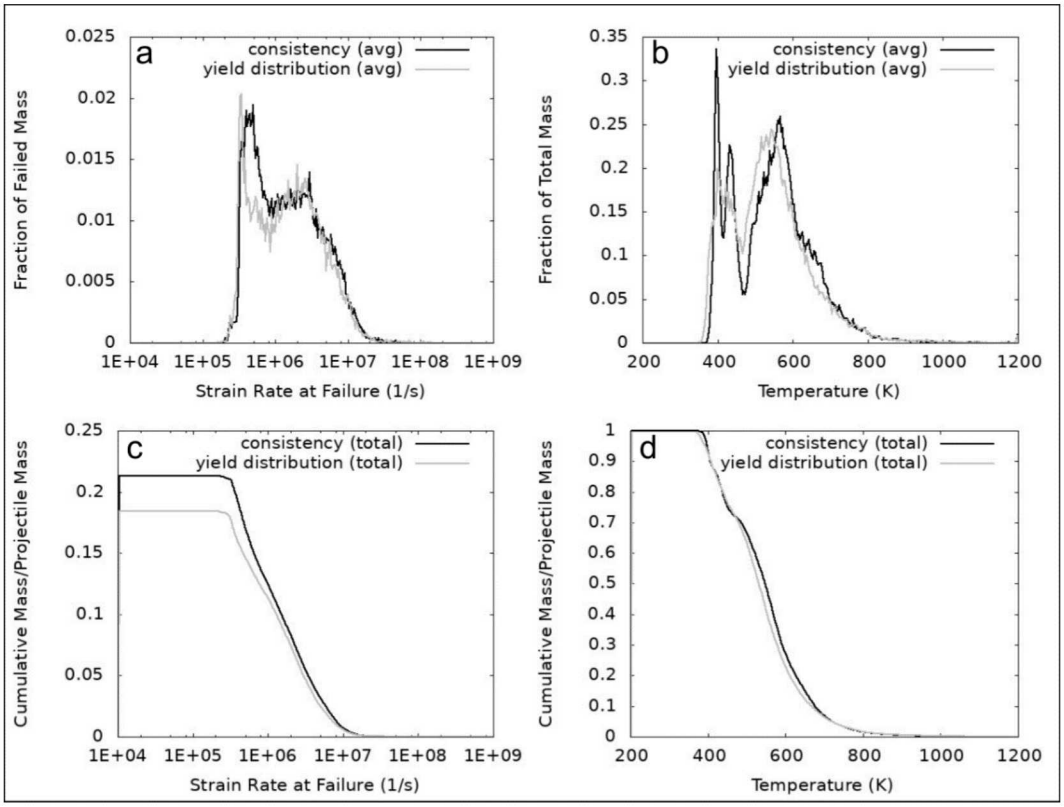

Figure 13 - Yield Strength Study Results (Projectile). Comparison of the grains consistency case (black line) with the results from using a yield strength distribution in the grains, in addition to the fracture strength distribution discussed in Section 3.2.2 (gray line). Histograms for (a) strain rate at failure and (b) material temperature compared to equivalent scaled cumulative mass plots of (c) strain rate at failure and (d) material temperature. A yield strength distribution in the grains predominantly affects only the first peak in the strain rate at failure histogram and results in less material at lower strain rates (as seen in the corresponding CDF). Material temperatures are somewhat decreased.

3.2.4 Slip Study

In the cases described above, the grains were treated as if they were cemented together. The slip study attempted to allow the grains to slide freely past one another. Two algorithms are available in CTH that allow this kind of behavior. The first is the Boundary Layer Interface (BLINT) algorithm. BLINT works on pairs of materials; one material is identified as "hard" and the other is identified as "soft." The hard material is allowed to slide past the soft material. Alternatively, the SLIDE option allows two materials to slide by one another by setting the shearing velocity gradients to zero (i.e., simulates discontinuous velocity across a sliding surface). Again, SLIDE works on pairs of material [26].

BLINT and SLIDE were used in two separate sets of simulations. Each material in the target and the projectile was paired with every other material (i.e., material 1 – material 2, material 1 – material 3, material 1 – material 4, etc.) to ensure all possible combinations were included such that any possible slip surface was represented.

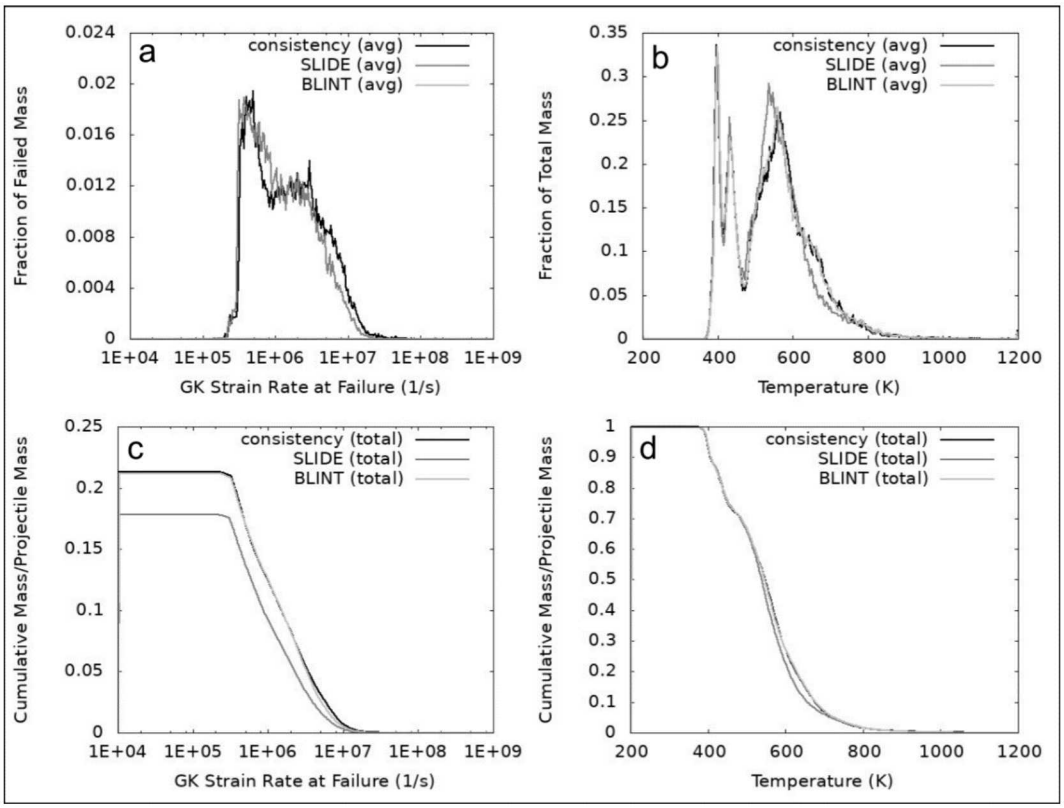

Figure 14 - Slip Study Results (Projectile). Comparison of the grains consistency case (black line) with the results from using a slip interface algorithm between the grains. The CTH SLIDE algorithm (dark gray line) is compared with the CTH BLINT algorithm (light gray line). Histograms for (a) strain rate at failure and (b) material temperature compared to equivalent scaled cumulative mass plots of (c) strain rate at failure and (d) material temperature. BLINT results closely match the consistency test, while SLIDE results in less failed mass, lower strain rates, and only slight changes to temperature.

From Figure 14, it is clear that neither SLIDE nor BLINT resulted in producing higher strain rates at failure or material temperatures than the consistency test. In fact, BLINT nearly exactly matched the consistency test. These results suggest that, at the kinds of strain

rates created in hypervelocity impacts, treatment of material interfaces plays a smaller role in the overall response than expected. However, known issues exist in these slip algorithms, which may have contributed to the inconsistency of the results of this study. Alternatively, the result may be because the grain boundaries perfectly matched each other, which had the consequence of negating any sliding boundary effect. Additional tests are required to draw conclusions regarding slip interfaces.

3.2.5 Interface Study

Finally, the last suite of simulations explored the role of grain interfaces in different manner than the slip study, above. Here, random grain interfaces were forced into the substructure of both the projectile and target. In the current problem description, the simplest and most consistent way to introduce these interfaces was to insert void into the problem by removing all grains of a single grain type from the calculation. The removal of a single grain type was computationally easy to perform by simply leaving one material undefined; however, this method resulted in 12.5% void space in the model. It is well understood that 12.5% porosity is uncharacteristic of metals, but the introduction of void is not intended to represent a realistic metal. Instead, the goal is to introduce interfaces throughout the problem at grain-void boundaries that are expected to be similar to interfaces that could result from imperfect grain-to-grain boundaries, discontinuities, and inclusions within the material [15].

The CTH pressure plot in Figure 15 visualizes the effects of void space on pressure with a comparison of plots for the consistency test (a) and the interface study (b). Void space clearly dampens the shockwave. Multiple rarefactions are seen within the grains of the target and projectile, which result in locally higher pressures than in the consistency test.

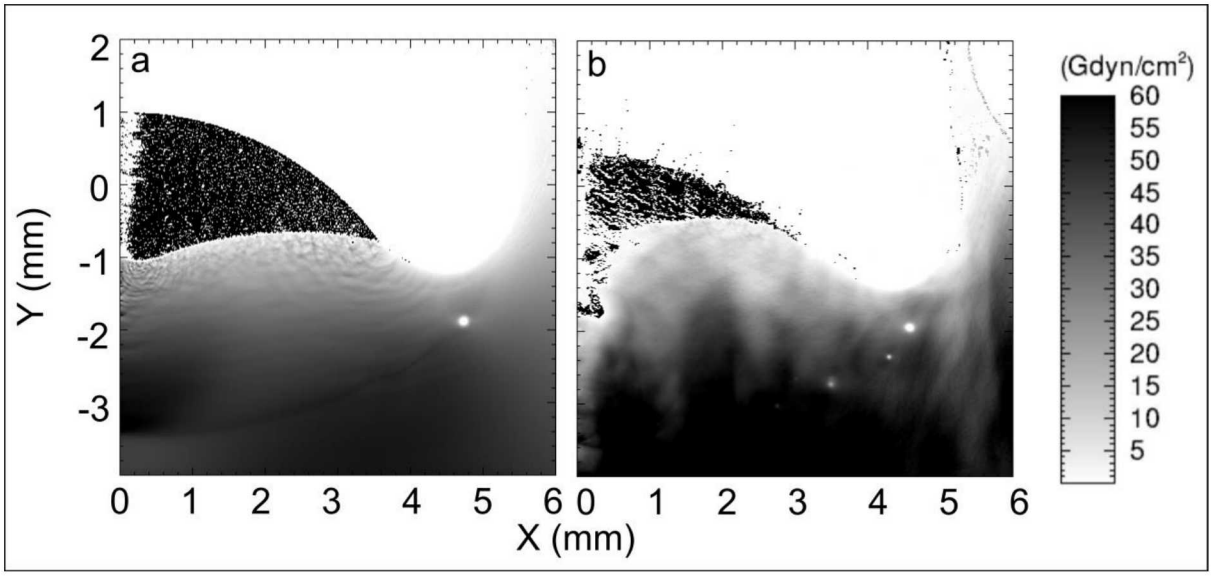

Figure 15 - CTH pressure plot (painted over the black projectile) for (a) the grains consistency test and (b) the porosity test. Void space clearly dampens the shockwave and multiple rarefactions are seen within the grains of the target and projectile. These shocks and rarefactions are believed to lead to locally higher strain rates at failure and material temperatures (Figure 16 and Figure 17).

Interfaces introduced because of void space result in substantial deviation from the grains consistency studies in strain rate at failure and material temperature. Plots for both the projectile and target (Figure 16 and Figure 17, respectively) demonstrate this deviation. The histogram for strain rate at failure nearly loses its bimodal shape in the projectile and shifts to higher strain rates in both the projectile and the target. This shift indicates that the projectile size is no longer the dominant property controlling the strain rate at failure. Instead, the smaller length scale of the individual grains become more important. The increase in both strain rate at failure and material temperature is likely due to the passage of several shock and rarefaction waves through the grains as they reflect off free surfaces produced by the voids.

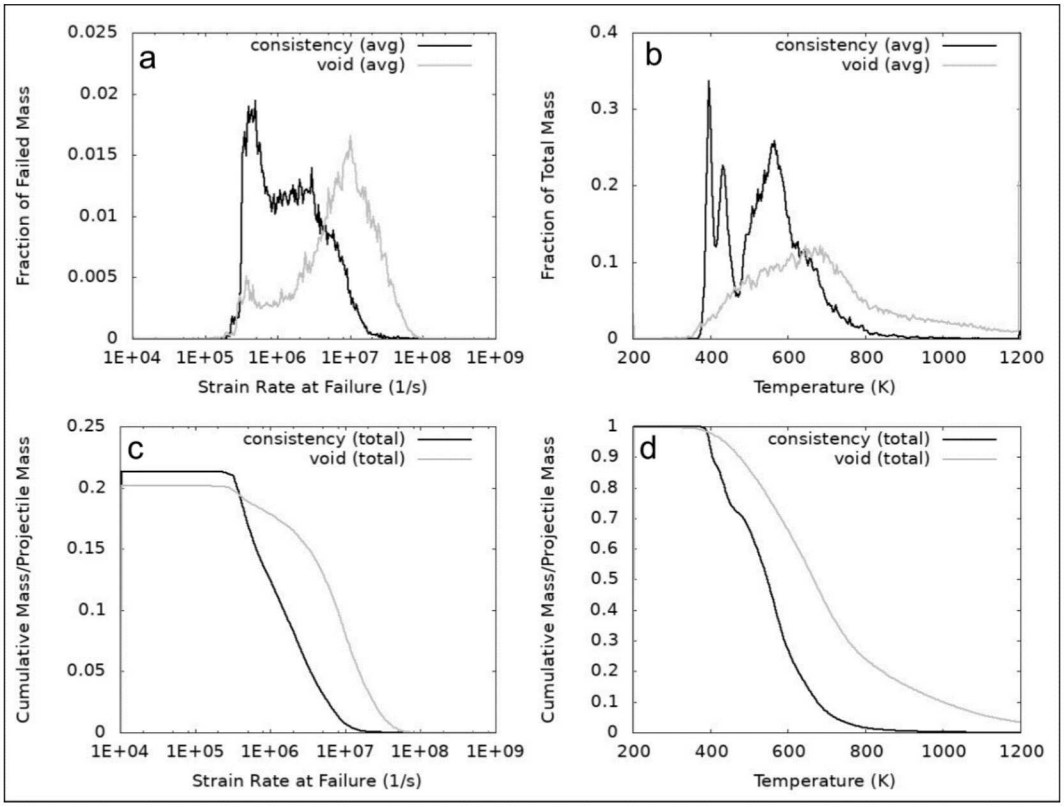

Figure 16 - Porosity Study Results (Projectile). Comparison of the grains consistency case (black line) with the porosity results (gray line). Histograms for (a) strain rate at failure and (b) material temperature compared to equivalent scaled cumulative mass plots of (c) strain rate at failure and (d) material temperature. The addition of void significantly affects both strain rate at failure and material temperature by shifting them both to higher values. This result is expected to affect EO/IR signatures.

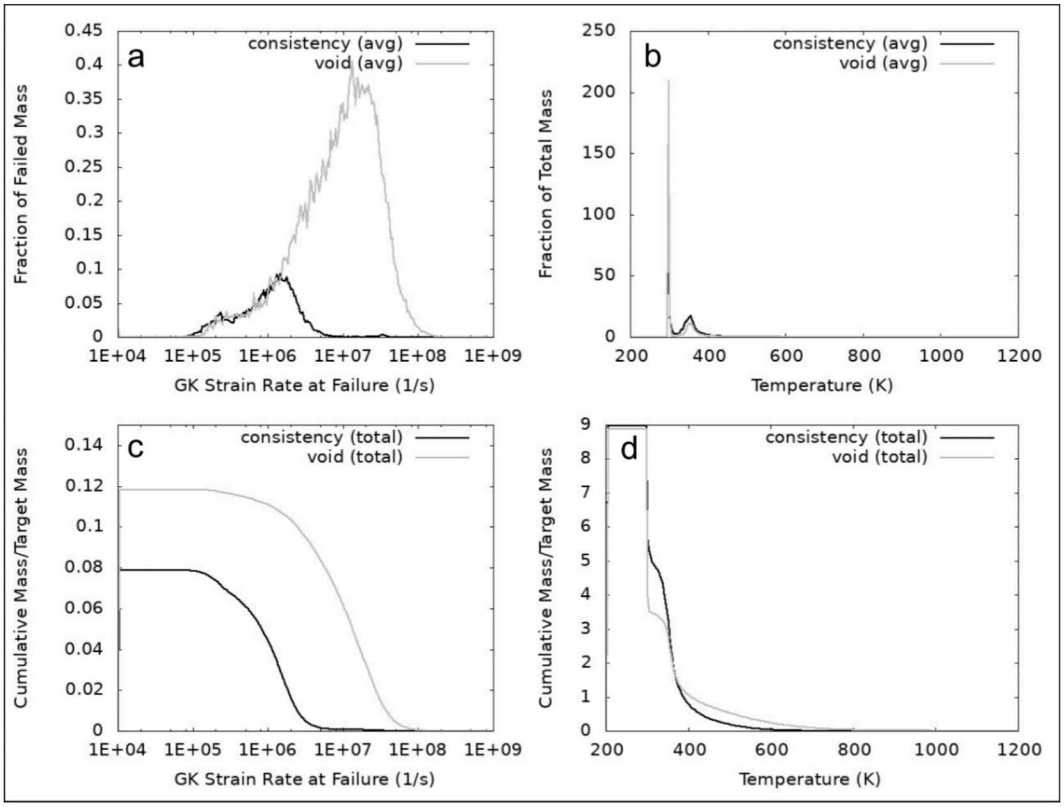

Figure 17 - Porosity Study Results (Target). Comparison of the grains consistency case (black line) with the porosity results (gray line). Histograms for (a) strain rate at failure and (b) material temperature compared to equivalent scaled cumulative mass plots of (c) strain rate at failure and (d) material temperature. The addition of void significantly affects both strain rate at failure and material temperature by shifting them both to higher values. More material failed in the target in the void case than in the consistency case.

3.2.6 Summary

In summary, attempts to change material properties or interface behavior between grains had only a minor effect, primarily only at low strain rates at failure (the first peak in the histograms). The second histogram peak for strain rate at failure remained nearly unchanged, which lends support to the hypothesis that a material property such as sound speed (unchanged in these studies) is a contributing factor to the production of higher strain rates. Results suggest that, for the values considered here, neither internally variable fracture strength nor yield strength are expected to significantly affect fragment size, material temperature, or the resulting EO/IR signatures. However, future studies should consider a

wider distribution of initial parameters (randomly picked fracture strengths or Johnson-Cook material properties), as well as simulations with different materials, in order to confirm the trends observed here.

The void-interface study was the only one to demonstrate an exceptional change in both the strain rate at failure and material temperature histograms and CDFs. Interfaces within a material (here, manifested as void space) are an important controlling factor for both strain rate and temperature during an impact. If the results presented here were to hold true for other types of interfaces besides void, and for a variety of impact speeds and conditions, a set of factors could be obtained by which to scale bulk, system-level results. A scaling factor would negate the need to run computationally expensive mesoscale models but would still allow system-level simulations to reflect the results described here.

Take, for example, the projectile in the void-interface study. The peak of the strain rate histogram (the largest percentage of failed mass) of the interface test is 20 times higher than that for the consistency test. If instead only the second strain rate histogram peak is used, the interface peak is still 3.4 times higher than the consistency test. Similarly, the peak in the interface test temperature histogram (the largest percentage of failed mass) is 1.2-1.7 times higher than the consistency test counterpart, depending on whether the peak at 400 K or 560 K is used. Scaling factors such as these could help system-level simulations produce higher strain rates and temperatures (small, hot debris fragments) through post-processing, which is currently required by many EO/IR predictive models to successfully compare with observed data.

4. CONCLUSION AND FUTURE WORK

The CTH shock physics code has been used to develop a detailed study of the effects of modeling the mesoscale grain structure of aluminum. Most system-level hypervelocity impact simulations use only a bulk description for materials, but such simulations tend to underestimate the resulting EO/IR signatures because they fail to produce enough small, hot debris. This study addressed what factors may control strain rate at failure (as a proxy for fragment size) and material temperature in both a traditional bulk modeling study and a mesoscale grain modeling study.

The bulk modeling suite was developed to baseline results from explicitly modeling grain structure. Grains were introduced to allow for internal variation of material properties in a given geometry (projectile or target). Nearly all attempts to change these material properties (fracture pressure, yield strength, or grain interface algorithms) produced only minor differences in low strain rates at failure and almost no major changes in material temperature when compared to the nominal consistency test. The introduction of material interfaces through the insertion of void, however, had a substantial effect.

Mesoscale modeling is computationally expensive and impractical for real, system-level simulations. The intent of this work is not to suggest that system-level simulations incorporate mesoscale structure, nor is it to calibrate the effect of grain structure yet. Instead, this work applies the idea of mesoscale modeling to the grain structure of metals in an attempt to gain an understanding of the underlying physics of grain interactions. While the interpretation of the results presented here are qualitative because the simulations are only 2D, the results demonstrate that some properties of the mesoscale grain structure may have a significant effect on EO/IR signatures. The goal was not to quantify how the mesoscale grain structure affects resulting signatures, although basic estimates were made to demonstrate the significance of the findings; rather, the study proposed a possible physical explanation for the

apparent mismatch in experimental EO/IR signatures and debris size. Interfaces between grains, such as those generated with the introduction of void, demonstrated a significant change in material response that is worth further study.

Future studies will confirm the results obtained here by expanding the work to three dimensions. While void space on the order of that described here is unrealistic, other material properties such as inclusions or dislocations may produce a similar result. Therefore, an investigation of other material interfaces, as well as non-1:1 grain aspect ratios, is warranted. The focus of future work will be how to calibrate the mesoscale response and incorporate it into the standard (bulk) method of material modeling in CTH. For example, a set of scaling factors could be developed to help computational models match observed EO/IR signatures.

DECLARATION OF COMPETING INTEREST

None.

ACKNOWLEDGEMENTS

The authors wish to thank Torch Technologies (specifically Jim Burke, Steven Henke, and Karen Hirsch) for supporting this work and providing insightful discussions about the results. This research did not receive any specific grant from funding agencies in the public, commercial, or not-for-profit sectors. This paper describes objective technical results and analysis. Any subjective views or opinions that might be expressed in the paper do not necessarily represent the views of the U.S. Department of Energy or the United States Government. Sandia National Laboratories is a multimission laboratory managed and operated by National Technology & Engineering Solutions of Sandia, LLC, a wholly owned subsidiary of Honeywell International Inc., for the U.S. Department of Energy's National Nuclear Security Administration under contract DE-NA0003525.

REFERENCES

[1] Barnes JP, Taylor EM, Mehta N. Micro-debris evolution from a satellite collision. In: AERO '11 Proceedings of the 2011 IEEE Aerospace Conference. 2011. https://doi.org/10.1109/AERO.2011.5747301.

[2] Rainey E, Stickle AM, Ernst CM, Schultz PH, Mehta NL, Brown RC, et al. Impact flash physics: modeling and comparisons with experimental results. In: American Geophysical Union, Fall Meeting, 2015, Abstract No. P53C-2131. 2015.

[3] Kipp ME, Grady DE. Dynamic fracture growth and interaction in one dimension. J of the Mechanics and Physics of Solids 1985; 64:399-415. https://doi.org/10.1016/0022-5096(85)90036-5.

[4] Glenn LA, Gommerstadt BY, Chudnovsky A. A fracture mechanics model of fragmentation. J App Phy 1986; 60: 1224. https://doi.org/10.1063/1.337373.

[5] Glenn LA, Chudnovsky. Strain-energy effects on dynamic fragmentation. J App Phy 1986; 59: 1379. https://doi.org/10.1063/1.336532.

[6] Zhou F, Molinari J-F, Ramesh KT. Effects of material properties on the fragmentation of brittle materials. Int J Fracture 2006; 139: 169-96. https://doi.org/10.1007/s10704-006-7135-9.

[7] Muelbroek, JP. The failure and fragmentation of ductile materials (Doctoral dissertation). The Johns Hopkins University. 2011.

[8] Grady DE. The spall strength of condensed matter. J Mech Phys Solids 1988; 36: 353-84. https://doi.org/10.1016/0022-5096(88)90015-4.

[9] Grady DE, Dunn JE, Wise JL, Passman SL. Analysis of prompt fragmentation. Sandia National Laboratories Report, SAND90-2015. 1990a.

[10] Grady DE, Swegle JW, Ang JA. Analysis of prompt fragmentation. Sandia National Laboratories Report, SAND91-0483. 1990b.

[11] Kipp ME, Grady DE, Swegle JW. Numerical and experimental studies of high-velocity impact fragmentation. Int J Impact Engng 1993; 14: 427-38. https://doi.org/10.1016/0734-743X(93)90040-E.

[12] Grady DE, Kipp ME. Impact failure and fragmentation properties of metals. Sandia National Laboratories Report, SAND98-0387. 1998.

[13] Borg JP, Vogler TJ. Mesoscale calcualtions of the dynamic behavior of a granular ceramic. Int J Solids Struct 2008; 45: 1676-96. https://doi.org/10.1016/j.ijsolstr.2007.10.027.

[14] Baer MR. Modeling of shocks in heterogeneous reactive materials. In: Horie Y, editor. Shock wave science and technology reference library, volume 2, New York: Springer; 2007, p. 321-51.

[15] Dwivedi SK, Asay JR, Gupta YM. Two-dimensional mesoscale simulations of quasielastic reloading and unloading in shock compressed aluminum. J App Phy 2006; 100: 083509. https://doi.org/10.1063/1.2357415.

[16] Case S, Horie Y. Modeling the shock response of polycrystals at the mesoscale. In: AIP Conference Proceedings 845. 2006. https://doi.org/10.1063/1.2263323.

[17] McGlaun JM, Thompson SL, Elrick MG. CTH: a three-dimensional shock wave physics code. Int J Impact Engng. 1990; 10: 351-60. https://doi.org/10.1016/0734-743X(90)90071-3.

[18] Hertel ES, Bell RL, Elrick MG, Farnsworth AV, Kerley GI, McGlaun JM, et al. CTH: a software family for multi-dimensional shock physics analysis. In: Brun R, Dumitrescu LZ, editors. Shock Waves @ Marseille I, Springer, Berlin, Heidelberg; 1993, p. 377-82. https://doi.org/10.1007/978-3-642-78829-1_61.

[19] Nakai M, Itoh G. The effect of microstructure on mechanical properties of forged 6061 aluminum alloy. Materials Transactions. 2014; 55: 114-9. https://doi.org/10.2320/matertrans.MA201324.

[20] Pierazzo E, Collins G. A brief introduction to hydrocode modeling of impact cratering. In: Dypvik H, Burchell MJ, Claeys P, editors. Craterin in Marine Environments and on Ice. Springer, Berlin, Heidelberg; 2004, p. 323-42. https://doi.org/10.1007/978-3-662-06423-8_16.

[21] Schultz, PH. Effect of impact-induced shear heating on vaporization and melting. In: Abstracts of the Lunar and Planetary Science Conference. 1995; 26:1249.

[22] Hafez Haghighat SM, Karimi Taheri A. An analytical and experimental investigation on the normal grain growth in metals using the Monte Carlo method. Materials & Design. 2007; 28: 2533-9. https://doi.org/10.1016/j.matdes.2006.09.006.

[23] Grain Size in Pure Aluminum, Image Analysis Report 262, Clemex, May 2013.

[24] Johnson GR, Cook WH. A constitutive model and data for metals subjected to large strains, high strain rates, and high temperatures. In: Seventh International Symposium on Ballistics, The Hague, Netherlands. 1983, p. 541-7.

[25] Silling SA. CTH reference manual: viscoplastic models. Sandia National Laboratories Report, SAND91-0292. 1996.

[26] Schmitt RG, Crawford DA, Harstad EN, Hensinger DM, Ruggirello KP. CTH user's manual and input instructions, Version 12.0. Sandia National Laboratories, Albuquerque, NM. 2017.

[27] Gray III GT, Chen SR, Wright W, Lopez MF. Constitutive equations for annealed metals under compression at high strain rates and high temperatures. Los Alamos National Laboratory Report, LA-12669-MS. 1994.